

1 **Modulation of the Indian Monsoon by Cross-Equatorial Ocean Heat**

2 **Transport**

3 Nicholas J. Lutsko*

4 *Department of Earth, Atmospheric, and Planetary Sciences, Massachusetts Institute of
5 Technology, Cambridge, Massachusetts*

6 John Marshall

7 *Department of Earth, Atmospheric, and Planetary Sciences, Massachusetts Institute of
8 Technology, Cambridge, Massachusetts*

9 Brian Green

10 *Department of Earth, Atmospheric, and Planetary Sciences, Massachusetts Institute of
11 Technology, Cambridge, Massachusetts*

12 *Corresponding author address: Nicholas Lutsko, Department of Earth, Atmospheric, and Planetary Sciences, Massachusetts Institute of Technology, Cambridge, Massachusetts

13 E-mail: lutsko@mit.edu

ABSTRACT

15 The role of the ocean circulation in modulating the Indian Monsoon is ex-
16 plored in an idealized study in which an atmospheric model is coupled to a
17 slab ocean with an interactive representation of ocean heat transport (OHT).
18 Summertime southwards ocean heat transport in the cross-equatorial cells of
19 the northern Indian Ocean (NIO) is found to play a critical role in increasing
20 the reversed meridional surface gradient of moist static energy, shifting the
21 precipitation maximum over land. This OHT is caused by Ekman flow driven
22 by the southwesterly monsoon winds, and results in cooling of sea-surface
23 temperatures (SSTs) of the NIO. The magnitude of the OHT can be systemat-
24 ically varied in the model, allowing the influence of OHT on the monsoon to
25 be studied. “Land” is added through use of a much reduced mixed-layer depth,
26 and hence heat capacity. It is found that OHT strengthens the monsoon, by en-
27 hancing the vertical wind shear and the precipitation over the land. However,
28 at the same time, the cross-equatorial mean meridional overturning circula-
29 tion is weakened, since less energy needs to be transported across the equator
30 by the atmosphere. The sensitivity of these effects to fixing the OHT at its
31 annual-mean value and to removing the land are also explored. A comparison
32 with observations suggests that the model produces a reasonable representa-
33 tion of the effects of OHT on the SSTs south of the continent, and if anything
34 underestimates the effects of OHT.

³⁵ **1. Introduction**

³⁶ It is now well understood that the South Asian Monsoon is a thermally-direct circulation driven
³⁷ by the thermodynamic contrast which develops in the summer months between the Indian subcon-
³⁸ tinent and the Indian Ocean to the south (e.g., Plumb and Hou (1992); Privé and Plumb (2007a);
³⁹ Privé and Plumb (2007b); Bordoni and Schneider (2008); Zhai and Boos (2015); Geen et al.
⁴⁰ (2018)). Intuitively, this contrast arises because the land’s smaller heat capacity causes it to warm
⁴¹ up faster in the summer than the surrounding waters, but recent work has shown that a number of
⁴² other factors are required to maintain the gradient. Most importantly, the Himalayas play a crucial
⁴³ role by insulating the Indian subcontinent from cold northerly winds blowing down from central
⁴⁴ Eurasia, keeping the surface temperatures high there during summer (see Boos and Kuang (2010)
⁴⁵ and Ma et al. (2014)).

⁴⁶ The other side of the contrast – the relatively cool waters of the northern Indian Ocean (NIO) –
⁴⁷ has been less explored. Privé and Plumb (2007b) compared the monsoons in simulations with their
⁴⁸ idealized atmospheric model forced by uniformly warm sea surface temperatures (SSTs) and by
⁴⁹ an SST profile that has a meridional gradient, and found that a meridional SST gradient promotes a
⁵⁰ cross-equatorial monsoon circulation. This picture was complicated, however, because the land in
⁵¹ their idealized set-up is cooled by zonal winds coming from the colder waters adjacent to the land,
⁵² damping the thermal contrast and hence the monsoon circulation (see also Chou et al. (2001)).
⁵³ Privé and Plumb were able to strengthen the monsoon in their model by adding “walls” around the
⁵⁴ continent to insulate it from these sea-breezes.

⁵⁵ While this provided a first indication of the relationship between the NIO and the monsoon cir-
⁵⁶ culation, it was highly idealized and did not consider feedbacks between the monsoonal winds and
⁵⁷ the SSTs. Webster and co-authors have suggested that the monsoon acts as a self-regulating sys-

tem (Loschnigg and Webster (2000); Webster et al. (2002); Chirokova and Webster (2006)), with strong monsoonal winds driving southward ocean heat transport (OHT) in the NIO, cooling the waters adjacent to the Indian subcontinent and hence damping the monsoon. This can be seen in observations, as the surface winds are southwesterly over the NIO in the summer and southeasterly south of the equator (arrows in Figure 1). The circulation pattern drives southward Ekman flow in the NIO’s mixed-layer, transporting heat into the southern hemisphere and potentially cooling the SSTs of the NIO. The heat transport can be inferred from the contours in Figure 1, which show the flux of heat from the atmosphere into the ocean. Developing a better understanding of the connection between OHT and the monsoon is the primary aim of this study.

The role of the Indian Ocean in cross-equatorial heat transport, but perhaps not monsoon dynamics, has been appreciated as far back as at least Levitus (1987). He hypothesized that the Ekman response to near surface equatorial winds in the Indian Ocean resulted in southward cross-equatorial heat transport in the boreal summer, which reversed in the winter. Ideas that describe the dynamical process involved, those of the Cross Equatorial Cell, are developed in McCreary et al. (1993), whose model was adapted by Loschnigg and Webster (2000) and Chirokova and Webster (2006).

Separate from the question of monsoons, the relationship between the zonal-mean atmospheric circulation and OHT has been investigated in a number of recent studies. It has been shown that including interactive OHT in idealized models substantially damps the Hadley circulation (Levine and Schneider (2011); Singh et al. (2017)), as well as meridional shifts of the intertropical convergence zone (ITCZ, Green and Marshall (2017); Schneider (2017)). The reason for this is that, because the weak Coriolis force at low latitudes means that large temperature gradients cannot be maintained away from the surface (Sobel et al. 2001), the tropical atmosphere is an inefficient transporter of energy. By contrast, the wind-driven subtropical cells in the ocean efficiently trans-

82 port energy away from the equator because of the large surface temperature difference between
83 the tropics and subtropics, which is mapped onto the vertical via subduction (Held (2001); Czaja
84 and Marshall (2005); Green and Marshall (2017)). Hence including interactive OHT means that
85 much less energy needs to be transported to high latitudes by the atmosphere. These studies have
86 focused on the zonal-mean perspective, but similar considerations would be expected to apply to
87 zonally-localized perturbations, such as monsoons, with the caveat that we do not yet have a good
88 understanding of what controls the partitioning between zonal and meridional energy transports.

89 Putting these results together, coupling to the ocean has a number of competing effects on the
90 monsoonal circulation, potentially strengthening it by enhancing the land-sea temperature gradient
91 and weakening it by cooling the waters adjacent to the land and by reducing the energetic
92 requirements on the cross-equatorial circulation. In this study we aim to untangle these effects by
93 investigating how the monsoon in a moist, gray radiation atmospheric general circulation model
94 (GCM) is affected by coupling the GCM to a slab ocean with an interactive representation of OHT.

95 The parameterization includes an ocean stratification parameter that can be varied to directly control
96 the strength of the OHT, allowing us to systematically investigate the influence of OHT on the
97 monsoon. We have also performed sensitivity experiments without land and with the OHT fixed at
98 its annual-mean value to separate zonally-asymmetric effects from zonal-mean effects and to cut
99 the coupling between OHT and the monsoonal circulation.

100 We note that our focus is primarily on the seasonal-mean monsoon and not on its variability.
101 Work with observations and comprehensive models has demonstrated a strong link between the
102 variability of the monsoon and SSTs in the Bay of Bengal; for instance, colder SSTs in the Bay
103 of Bengal precede monsoon “breaks”, periods when the rains are muted, by about a week (e.g.,
104 Vecchi and Harrison (2002); Schott et al. (2009)). However this variability is unlikely to be well
105 represented in our model because of the idealized geometries we use and also because the GCM

106 does not include a representation of clouds. As such our focus is on the mean state of the monsoon,
107 which our model can be expected to represent, and on the more general question of the relationship
108 between the zonally-asymmetric atmospheric circulation and OHT.

109 The model and the simulations we have performed are described in more detail in the next
110 section. In section 3 we investigate how the monsoon in our model is affected by coupling with
111 the OHT, including how it is affected by varying the strength of the OHT and by fixing the OHT
112 at its annual-mean value. In section 4 we compare the model with observations to assess how
113 relevant our results may be for the real South Asian Monsoon and in section 5 we present the
114 results of the experiments without land. We end with conclusions in section 6.

115 2. Model Description and Simulations

116 The model consists of the idealized moist GCM first described by Frierson et al. (2006), coupled
117 to a slab ocean with an idealized representation of OHT by the subtropical cells.

118 a. The Moist GCM

119 The GCM solves the primitive equations on the sphere and is forced by gray radiation. The long-
120 wave optical depth is specified to approximate the effects of atmospheric water vapor (Frierson
121 et al. 2006):

$$\tau(p, \phi) = \tau_0 \left[f_l \left(\frac{p}{p_s} \right) + (1 - f_l) \left(\frac{p}{p_s} \right)^4 \right], \quad (1)$$

122 where p is pressure, ϕ is latitude, p_s is the surface pressure and the linear term is included to
123 reduce stratospheric relaxation times (f_l is set to 0.1). τ_0 is the optical depth at the surface, and
124 takes the form

$$\tau_0(\phi) = \tau_{0e} + (\tau_{0p} - \tau_{0e}) \sin^2 \phi, \quad (2)$$

125 with τ_{0e} the surface value at the equator and τ_{0p} the surface value at the pole. These are set to 7.2
 126 and 1.8, respectively (O’Gorman and Schneider 2008). The solar insolation has an annual cycle,
 127 but no diurnal cycle, and is calculated as (see chapter 2 of Hartmann (2016)):

$$S_0 = \frac{S_c}{\pi} [h_0 \sin\phi \sin\delta + \cos\phi \cos\delta \sin h_0], \quad (3)$$

128 where the solar constant S_c is set to 1360 W m^{-2} ; h_0 is the longitude of the subsolar point at sunrise
 129 and sunset relative to its position at noon; and δ is the declination, calculated using an obliquity
 130 of 23.45° , a 360 day year and assuming that Earth’s orbit is perfectly circular. The albedo is fixed
 131 at 0.38 and the absorption of solar radiation by the atmosphere is modelled by calculating the
 132 downward shortwave flux at a given pressure level as $S = S_0 \exp(-\tau_s(p/p_s)^2)$, with τ_s fixed at
 133 0.22, as used by O’Gorman and Schneider (2008).

134 The model includes the simplified Betts-Miller (SBM) convection scheme of Frierson (2007),
 135 with a convective relaxation time-scale τ_{SBM} of 2 hours and a reference relative humidity RH_{SBM}
 136 = 0.7, and the boundary layer scheme is the one used by O’Gorman and Schneider (2008). In
 137 each experiment the model was integrated for four years at T85 truncation (corresponding to a
 138 resolution of roughly 1.4° by 1.4° on a Gaussian grid) with 30 vertical levels extending up to
 139 16hPa. Averages were taken over the last three years of each simulation.

140 b. Interactive OHT parameterization

141 OHT can be represented as the product of a meridional overturning circulation and an energy
 142 contrast (Held (2001); Czaja and Marshall (2005))

$$q_O = c_{p,o} \Phi \Delta T, \quad (4)$$

143 where $c_{p,o}$ is the heat capacity of seawater, Φ is the overturning mass transport streamfunction
 144 and ΔT is the temperature difference across the upper and lower branches of the overturning cir-

¹⁴⁵ culation, i.e., between the top and base of the subtropical cells. This can also be thought of as
¹⁴⁶ the surface temperature difference between the deep tropics and the latitude of subduction, with
¹⁴⁷ typical values of 5-10K (Klinger and Marotzke 2000).

¹⁴⁸ In the tropics, the oceanic mass transport is mostly set by the Ekman mass transport, allowing
¹⁴⁹ us to approximate the OHT as

$$q_O(\phi, \lambda) \approx ac_{p,o} \cos\phi \frac{\tau(\phi, \lambda)}{f(\phi)} \Delta T, \quad (5)$$

¹⁵⁰ where λ is longitude, a is the radius of the Earth, τ is the wind stress and f is the Coriolis parameter.
¹⁵¹ The interactive OHT parameterization assumes that heat is only transported via equation 5, and
¹⁵² only calculates the OHT for latitudes between ϕ_1 , the latitude at which the surface winds change
¹⁵³ from westerly to easterly in the southern hemisphere, and ϕ_2 , the latitude at which the surface
¹⁵⁴ winds change from easterly to westerly in the northern hemisphere. $c_{p,o}$ is set to $3900 \text{ J kg}^{-1} \text{ K}^{-1}$
¹⁵⁵ and, importantly, ΔT is left as a free parameter to be specified.

¹⁵⁶ This parameterization is similar to the scheme used by Klinger and Marotzke (2000) and Levine
¹⁵⁷ and Schneider (2011), except that their scheme uses surface quantities, so that the OHT is calcu-
¹⁵⁸ lated from the surface wind and temperature fields, with no free parameters. Here we specify ΔT
¹⁵⁹ directly in order to systematically investigate how the strength of the OHT impacts the monsoon,
¹⁶⁰ as larger ΔT values result in more heat being transported southwards in the summer. Our scheme is
¹⁶¹ also similar to the “1.5-layer” parameterization of Ekman heat transport by Codron (2012), though
¹⁶² we have excluded diffusive heat transport and only focus on heat transport in the tropics.

¹⁶³ As in Levine and Schneider (2011), we apply a Gaussian smoothing filter when calculating the
¹⁶⁴ divergence of the heat flux to avoid issues with f going to zero at the equator:

$$(\nabla \cdot q_O)' = \int_{\phi_1}^{\phi_2} \frac{1}{a \cos\phi} (\nabla \cdot q_O) P(\phi, \phi') d\phi', \quad (6)$$

¹⁶⁵ where

$$P(\phi, \phi') = \frac{1}{Z} \exp\left(\frac{-(\phi' - \phi)^2}{2s^2}\right), \quad (7)$$

¹⁶⁶ with Z chosen such that the integral of P from ϕ_1 to ϕ_2 is equal to one and s a half-width, which is
¹⁶⁷ set to 7° .

¹⁶⁸ The depth of the ocean is fixed at 24m in all of our simulations. Donohoe et al. (2014) found
¹⁶⁹ that coupling the CM2.1 GCM to a 24m slab ocean produced a climate with a reasonable seasonal
¹⁷⁰ migration of the ITCZ compared with observations, and also a reasonable annual-mean Hadley
¹⁷¹ circulation and meridional distribution of precipitation.

¹⁷² “Land” is added to the model by reducing the mixed-layer depth to 0.5m and setting the ocean
¹⁷³ heat flux divergence to zero between 100° - 235° E and 15° - 40° N. This provides an infinite
¹⁷⁴ supply of moisture for the monsoonal circulation and also means that the global integral of q_o
¹⁷⁵ is not always zero. So there may be net OHT from the northern hemisphere into the southern
¹⁷⁶ hemisphere, even for conditions that are otherwise hemispherically-symmetric, however we find
¹⁷⁷ that in the annual-mean the ITCZ is very close to the equator in all of our simulations (not shown).

¹⁷⁸ The geometry of our set-up is illustrated in Figure 2.

¹⁷⁹ *c. Simulations*

¹⁸⁰ We have performed three sets of simulations with the model, motivated by our aim of untangling
¹⁸¹ the competing effects of OHT on the monsoon. The main set includes both land and the interactive
¹⁸² OHT, with ΔT varied from 0K (i.e., no OHT) to 15K. In a second set of simulations the OHT at
¹⁸³ each grid point is fixed at its annual-mean value from the first set of simulations, eliminating the
¹⁸⁴ coupling between OHT and the monsoonal circulation but maintaining the annual-mean effects of
¹⁸⁵ OHT. The third set include the interactive OHT but not the land, with ΔT again varied from 0K to

¹⁸⁶ 15K. Comparing these simulations with the first set of simulations allows the impacts of the OHT
¹⁸⁷ on the zonal-mean circulation to be separated out.

¹⁸⁸ **3. The Relationship Between OHT and the Model’s Monsoon**

¹⁸⁹ *a. Comparing Simulations With and Without OHT*

¹⁹⁰ We begin by comparing the monsoons in a simulation without OHT and a simulation with ΔT
¹⁹¹ = 10K, which is one of our more realistic simulations (see section 4). Figure 3 shows the sum-
¹⁹² mertime¹ precipitation and surface winds (top panels), the summertime surface moist static energy
¹⁹³ (middle panels) and the summertime ocean heat flux divergence for the interactive case (bottom
¹⁹⁴ right panel). The surface moist static energy is calculated as $c_p T + L_v q_v$, where c_p is the specific
¹⁹⁵ heat capacity of dry air, T is the temperature at the lowest model level, L_v is the latent heat of
¹⁹⁶ vaporization of liquid water and q_v is the specific humidity at the lowest model level.

¹⁹⁷ Without OHT, the ITCZ is slightly north of the equator, at about 5°N in the zonal-mean, and
¹⁹⁸ there is also a weak precipitation maximum just south of the continent. The surface MSE is
¹⁹⁹ relatively uniform throughout the tropics, though the largest values are on the southern edge of the
²⁰⁰ continent so that the highest precipitation in the land sector is substantially further equatorward of
²⁰¹ the MSE maximum. The winds resemble the observations (Figure 1), being southeasterly up to
²⁰² about 5°N and then swinging around to be southwesterly between 5°N and 20°N, but the winds
²⁰³ north of 5° are weak.

²⁰⁴ In the simulation with OHT there is much clearer evidence of a monsoon, with the highest
²⁰⁵ precipitation over the southern edge of the continent, at about 17°N. The winds again resemble
²⁰⁶ the observations, and are stronger between 5°N and 20°N than in the no OHT case. The surface
²⁰⁷ MSE is generally smaller than in the simulation without OHT, because the OHT parameterization

¹In the simulations we define “summer” as the 90 warmest days over the land and “winter” as the 90 coldest days over the land.

208 redistributes heat to the subtropics, and there is a sharper maximum in MSE over the continent,
209 resulting in a larger land-ocean contrast in low-level MSE. Panel e) of Figure 3 shows that the
210 ocean transports heat southwards across the equator, as well as from the tropics into the subtropics
211 of the Northern Hemisphere.

212 Figure 4 compares the seasonal cycles in precipitation (top panels) and surface MSE (bottom
213 panels) in these simulations, with values averaged over the land sector. Without OHT the maxi-
214 mum precipitation varies smoothly over the course of the year, following the maximum insolation,
215 though there is increased precipitation just south of the land in the late spring and summer months.
216 The MSE shows a similar progression, and the largest MSE is in the summer and early fall because
217 of the larger warming of the land.

218 The seasonal cycle of precipitation is less regular when OHT is included, and the maximum pre-
219 cipitation is weaker than in the simulation without OHT (panel c). Both the precipitation and the
220 maximum MSE jump to the warmer hemisphere during the transition seasons. The amplitude of
221 the seasonal cycle in MSE is larger in the Northern Hemisphere than in the Southern Hemisphere,
222 as the highest MSE values are found over the land in the summer months, while the lowest MSE
223 values are over the land in the winter months. This is discussed further in section 5.

224 *b. Varying ΔT*

225 The effects of varying the strength of the OHT on the surface climate of the model are summa-
226 rized in Figure 5. As ΔT is increased the tropical SSTs in the land sector cool and the meridional
227 SST gradient is reduced (panel a). However the land-ocean surface temperature contrast increases
228 dramatically, going from about 0.2K to 1.5K as ΔT is increased from 0K to 15K. The MSE has
229 a similar progression (panel b), though the profile is smoother, without such a sharp jump across
230 the land-ocean boundary, because of the specific humidity (panel d). A secondary MSE maximum

231 develops in the southern hemispheres of the experiments with large ΔT , due to a maximum in the
232 specific humidity.

233 The ITCZ is close to 5°N in the 0K and 2.5K simulations, before jumping over the land in the
234 5K simulation. This appears to be an intermediate case, as the ITCZs in the 10K and 15K are very
235 similar to each other. The OHT is also similar in these two simulations (panel e), suggesting that
236 it may saturate for large enough ΔT . Privé and Plumb (2007a) showed that precipitation maxima
237 will occur slightly equatorward of maxima in the surface MSE, where the meridional gradient in
238 surface MSE (to which the vertical wind shear is proportional) is largest. Although the maximum
239 MSE in the 0K and 2.5K cases is over the land, there are also MSE maxima near 5°N in these
240 simulations.

241 Figure 6 plots the zonal-winds in these simulations in black contours and the mean meridional
242 circulation (MMC) in the red contours. The MMC is calculated as $\frac{1}{g} \int_{p_s}^P \bar{v}(p', \phi) dp'$, where an
243 overbar denotes an average over the land sector. The overturning circulation expands and weakens
244 as ΔT is increased, while the vertical shear in the zonal wind, which is often taken as a proxy for the
245 strength of the monsoonal circulation (Webster and Yang 1992), increases. This is primarily due
246 to a strengthening of the easterlies near the tropopause. For larger ΔT a jump in the near-surface
247 meridional circulation develops just north of the equator because of the difficulty the return flow of
248 the Hadley circulation has in crossing the equator close to the surface when the equatorial surface
249 temperature gradient is weak (Pauluis 2004).

250 The round markers in Figure 7 quantify these changes by showing the maximum vertical zonal
251 wind shear ($u(850\text{hPa}) - u(250\text{hPa})$) between the equator and 20°N as a function of ΔT in panel a)
252 and the minimum (i.e., the most negative) values of the MMC as a function of ΔT in panel b). The
253 zonal wind shear increases slightly when going from 0K to 2.5K, then jumps at 5K and increases
254 roughly linearly as ΔT is increased further. Comparing with panel c) of the Figure shows that

255 this progression closely tracks the changes in the MSE gradient. In an angular momentum (AM)
256 conserving flow the zonal-wind shear is proportional to the subcloud MSE gradient (Emanuel
257 1995) and, though the flow in these simulations is far from the AM-conserving limit (see below),
258 we believe that this argument is still relevant here.

259 Conversely, the strength of the MMC decreases roughly linearly from 0K to 10K and then in-
260 creases slightly for $\Delta T = 15K$. The decrease over the first four simulations is expected from the
261 discussion in the introduction: as ΔT is increased the atmosphere has to transport less energy
262 across the equator and so the circulation slows down. A quantitative theory for the compensation
263 between energy transport by the Hadley circulation and OHT is still lacking, however, and in par-
264 ticular requires a better understanding of how the gross moist stability of the tropical atmosphere
265 is controlled (Singh et al. 2017).

266 Panel d) of Figure 7 shows the minimum absolute vorticity ($f + \zeta$, where f is the Coriolis
267 parameter and ζ is the relative vorticity) polewards of 7° during the summer of these simulations.
268 The absolute vorticity vanishes in the upper troposphere of an AM-conserving flow and, although
269 none of the simulations are close to this regime, there is a substantial decrease in the minimum
270 absolute vorticity, from about $0.55 \times 10^{-5} s^{-1}$ to $0.41 \times 10^{-5} s^{-1}$ when going from $\Delta T = 10K$
271 to $\Delta T = 15K$. This step towards an AM-conserving flow is caused by the increased vertical wind
272 shear, as the stronger upper-level easterlies shield the tropical circulation from baroclinic eddies
273 originating at mid-latitudes (Bordoni and Schneider 2008). Since these eddies act as a drag on
274 the mean flow, increased shielding may explain why the MMC strengthens in the $\Delta T = 15K$ case
275 (Walker and Schneider 2006).

276 In summary, increasing ΔT both strengthens the monsoonal circulation by increasing the land-
277 sea contrast and damps the monsoon because less heat needs to be carried across the equator by
278 the atmosphere.

279 c. Specifying the OHT

280 The effects of the OHT on the monsoon come partly from the seasonal variations in the OHT
281 and partly from the effects of the annual-mean OHT. Our second set of simulations separate these
282 out, as the OHT is fixed at the annual-mean profiles from the interactive experiments. The crosses
283 in the top panels of Figure 7 show that this increases the maximum zonal-wind shear and also the
284 MMC. The MSE gradient also increases (panel c), while the minimum absolute vorticity decreases
285 rapidly, so that the flow is approximately AM-conserving for $\Delta T = 10K$ and above (panel d).
286 While this transition to an AM-conserving regime will strengthen the flow somewhat, panel e) of
287 the Figure shows that in fact the MMC scales linearly with the OHT at the equator, so that the
288 energetic requirements on the Hadley circulation are the dominant control on its strength.

289 More insight into the effects of specifying the OHT on the monsoon comes from the left panels
290 Figure 8, which show the summer climate in the case with the OHT from the $\Delta T = 10K$ case. The
291 monsoon is stronger than in the corresponding case with interactive OHT, with stronger winds
292 and precipitation, as well as a larger land-sea MSE contrast. The shape of the winds means in
293 particular that the monsoon is strongest in the southeast corner of the continent. The reason for
294 this stronger monsoon can be seen by comparing panel e), which shows the OHT divergence
295 in this simulation, with panel e) of Figure 3. The annual-mean OHT is still southwards in the
296 land sector, but the ocean now converges heat at the latitudes of the south coast of the continent
297 ($15\text{--}20^\circ$), rather than diverging heat as it was in the interactive case. This warms the waters on
298 either side of the continent, so that the continent is not cooled as much by zonal breezes as it was
299 in the interactive case. This is reminiscent of how Privé and Plumb (2007b) found that adding
300 walls to their continent strengthened the monsoon by insulating it from zonal sea breezes (see
301 Introduction).

302 **4. Comparing with Observations**

303 The above results give an indication of how interactive OHT might affect the South Asian mon-
 304soon, however the idealized nature of our model makes it unclear how relevant our results are for
 305the real atmosphere. In particular, from the point of view of simulating seasonal variability, the
 306main drawback of the interactive OHT parameterization is that the mixed-layer depth (MLD) is
 307kept fixed. In the real ocean changes in OHT do not necessarily lead to changes in SSTs, because
 308the MLD may also deepen or shoal.

309 The heat budget for a volume of ocean water is

$$Q_S(t) = Q_O(t) + Q_F(t), \quad (8)$$

310 where Q_S is the change in heat stored in the volume:

$$Q_S(t) = a^2 \rho c_{p,0} \int_{MLD}^0 \int_{\phi_1}^{\phi_2} \int_{\lambda_1}^{\lambda_2} \frac{dT}{dt} \cos\phi d\lambda d\phi dz, \quad (9)$$

311 with ρ the density of seawater and T is the depth-averaged temperature of the mixed-layer. Q_O
 312 is the OHT (q_O) integrated around the lateral boundaries of the volume, as well as heat fluxed
 313 through the bottom of the mixed-layer (which we ignore) and Q_F is the surface heat flux into the
 314 water:

$$Q_F(t) = a^2 \int_{\phi_1}^{\phi_2} \int_{\lambda_1}^{\lambda_2} (Q_{SW} + Q_{LW} + Q_{LH} + Q_{SH}) \cos\phi d\lambda d\phi, \quad (10)$$

315 where Q_{SW} is the incoming solar radiation at the surface, Q_{LW} is the outgoing longwave radiation
 316 at the surface, Q_{LH} is the surface latent heat flux and Q_{SH} is the surface sensible heat flux. Note
 317 that if Q_F is fixed then changes in Q_O can be compensated either by changes in T or by changes
 318 in the MLD and so since the MLD is fixed in our model changes in Q_O can only be compensated
 319 by changes in T .

320 Figure 9a shows the heat budget for the ocean off the coast of the continent (100° to 235° E
321 and 0 to 15° N) for the simulation with land and $\Delta T = 10$ K, which we consider to be one of our
322 most realistic simulations. The ocean carries heat north across the equator in winter and south in
323 summer, while it is warmed by the surface fluxes in summer and cooled in the winter. The largest
324 surface fluxes are in the spring and in the fall because the strong monsoon winds in the summer
325 lead to enhanced evaporative cooling over the ocean. These terms produce a seasonal cycle of
326 ~ 4 K in the SSTs (solid line in Figure 9b), with the warmest SSTs in the fall when the OHT and
327 the monsoonal winds are weaker.

328 These results agree qualitatively with previous studies of the heat budget of the NIO, though
329 there are some notable differences. Comparing with Figure 3 of Chirokova and Webster (2006),
330 the seasonal cycles of the OHT and of the surface fluxes in our simulations are similar to their
331 modelled NIO, except that the OHT is generally larger than the surface fluxes in their simulations
332 whereas the reverse is the case in our simulations (though we note that because of our idealized
333 set-up we are not averaging over the same geometries). The other major difference is that in their
334 simulations Q_F is almost zero during the summer and early fall, because increased cloudiness
335 reduces the solar radiation absorbed by the surface (as a reminder, there are no clouds in our
336 model) and because of stronger evaporative cooling than in our simulations caused by stronger
337 monsoonal winds. The large reduction in Q_F in the summer means that the warmest SSTs in the
338 NIO are actually in April and May (dashed line in Figure 9b), rather than in the fall.

339 Babu et al. (2004) showed that the MLD in the NIO is shallowest in February and March, which
340 contributes to the warm SSTs in the spring, and then deepens over the course of the summer due
341 to mixing caused by the monsoonal winds. The mixed-layer shoals rapidly again in the fall at
342 the end of the monsoon season and then deepens in the winter months. The gradual deepening
343 of the mixed-layer during the summer will damp the cooling of the NIO SSTs by OHT during

344 the summer months, but on the whole we believe that our model underestimates the cooling of
345 the NIO SSTs by OHT, and the amplitude of the seasonal cycle of SSTs in the NIO is smaller
346 than in our model (Figure 9b). So although there are differences between the heat budgets of our
347 model and in more realistic models due to the fixed mixed-layer depth in our model and the lack
348 of clouds, we believe that our model qualitatively captures the impact of OHT in the NIO on the
349 SSTs south of the Indian subcontinent.

350 **5. Zonal-Mean Effects**

351 The behavior discussed in section 3 comes from the monsoon generated over the land, but also
352 from the zonal-mean effects of the interactive OHT. We use our third set of experiments – with
353 interactive OHT but no land – to investigate how the interactive OHT affects the zonal-mean
354 circulation of the model.

355 The triangles in Figure 7a show that excluding the land reduces the vertical zonal wind shear by
356 roughly half, though this still increases as ΔT is increased and the MSE gradient also strengthens
357 (panel b). So, even without the land the southward energy transport by the ocean still produces
358 a monsoon-like circulation. The MMC is very similar with and without land (Figure 7b), as it is
359 mostly determined by the OHT (section 3.3).

360 These experiments, together with the fixed OHT experiments, can also be used to understand the
361 seasonal cycles in Figure 4. In the simulation without land and with $\Delta T = 10K$ there are actually
362 three maxima in the precipitation (Figure 10a), one close to the equator and one further polewards
363 in each hemisphere, with all three shifting gradually over the course of the year. A double-ITCZ
364 structure is expected because the OHT and the heat transport by the atmosphere result in the net
365 energy input to the deep tropics being negative (Bischoff and Schneider 2016), while the peak at

366 the equator is caused by rising motion as the meridional circulation jumps over the equator (not
367 shown).

368 The fixed OHT experiment resembles the original Hovmuller diagrams, but with the features
369 exaggerated (Figure 10c and f). In the winter there is very little precipitation in the northern hemi-
370 sphere and a strong maximum in precipitation at about -15°S. A strong maximum appears in the
371 northern hemisphere over the land in the spring, while the maximum in the southern hemisphere
372 weakens and gradually shifts to the north, joining the strong peak over the land in the late sum-
373 mer. During the fall the maximum slowly migrates southwards, before jumping further south once
374 winter sets in.

375 These jumps are primarily caused by strong surface winds blowing south off the continent in the
376 winter (Figure 8b). Because the continent is very cold in the winter, these winds cool the oceans
377 to the south of the continent, creating a strong meridional MSE gradient compared to the warmer
378 waters of the southern hemisphere (Figure 8d; note that the MSE near the equator is colder than
379 in the summer). These winds die down in the spring as the land, and the oceans to either side
380 of it, warm up, rapidly reducing the MSE gradient and causing a strong MSE and precipitation
381 maximum to develop over the continent. At the same time, the precipitation maximum in the
382 south migrates northwards, following the peak insolation, until it merges with the maximum over
383 the land. In the fall the land cools and the MSE maximum gradually migrates southwards until the
384 strong winds pick up again, rapidly cooling the ocean and causing the jump to the strong southern
385 precipitation maximum during winter.

386 We have performed an additional experiment without land and with the OHT fixed at its annual-
387 mean value from the no-land $\Delta T = 10\text{K}$ experiment. This is similar to the fixed OHT with land,
388 though the precipitation maxima are weaker (Figure 10b). The MSE is smallest in the transition
389 months (Figure 10e), when it has a minimum near the equator because the atmosphere and ocean

390 transport heat to higher latitudes, resulting in a double-ITCZ. In the summer and winter, the atmo-
391 sphere transfers heat into the tropics, so that they gain energy in the net (not shown) and there is a
392 single ITCZ.

393 Together, these can explain the features seen in Figure 4. The jumps in the precipitation max-
394 imum and in the MSE maximum come about because of the rapid warming and cooling of the
395 continent, but at the same time the interactive OHT often results in a double ITCZ, as there is net
396 energy transport out of the deep tropics.

397 **6. Conclusion**

398 In this study we have investigated the monsoon in an idealized model consisting of the widely
399 used gray-radiation atmospheric GCM, coupled to an idealized parameterization of ocean heat
400 transport by the subtropical cells. The OHT parameterization includes a parameter, ΔT , which can
401 be used to vary the strength of the OHT, allowing us to systematically investigate the impact of
402 OHT on the monsoon in this model.

403 Without OHT the monsoon in our model is weak, because the land surface is not protected
404 from cold winds coming either from further north or from the east and west of the land (see also
405 Chou et al. (2001) and Privé and Plumb (2007b)). However, by increasing ΔT sufficiently we are
406 able to create a reasonable monsoon circulation because the waters south of the land cool during
407 the summer, creating a strong meridional MSE gradient. This includes increases in the vertical
408 wind shear as ΔT is increased and in the precipitation over land, though the MMC weakens.
409 The shear strengthens because the meridional MSE gradient increases, while the MMC weakens
410 because the increased OHT means that the atmosphere is required to transport less heat across the
411 equator. For $\Delta T = 15\text{K}$ the vertical shear is strong enough to start pushing the flow towards an
412 angular momentum-conserving regime. Fixing the OHT at its annual-mean value results in the

413 OHT warming the waters zonally-adjacent to the land, rather than cooling them, as in the case
414 with interactive OHT, but the waters south of the land are still cooled as there is southwards OHT
415 in the land sector (Figure 8e). This increases the MSE gradient compared to the interactive case,
416 resulting in a stronger monsoon circulation, which causes the flow in the simulations with $\Delta T =$
417 10K and above to be in an AM-conserving regime. A comparison with observations and more
418 realistic models of the Northern Indian Ocean suggests that the effects of our parameterized OHT
419 on the SSTs south of the continent are reasonable, and if anything underestimate the effects of
420 OHT.

421 Combining the original experiments with the fixed OHT experiments and the experiments with-
422 out land showed that the changes in the MMC are largely due to changes in the OHT, with the
423 MMC weakening as the OHT increased. By contrast, the presence of land and/or of a transition to
424 an AM-conserving regime have minor impacts the MMC, except in so far as they effect the OHT.
425 Finally, the seasonal cycle of precipitation in the interactive OHT simulations exhibits jumps, as
426 strong precipitation suddenly appears over the continent in the summer and in the southern hemi-
427 sphere during winter. These jumps are even clearer in the simulations with fixed OHT, and are
428 caused by strong winds blowing off the continent during the winter months, which cool the waters
429 south of the continent and set-up a strong MSE maximum in the southern hemisphere. When the
430 land warms up sufficiently these winds stop and the waters north of the equator warm up quickly,
431 while an MSE maximum develops over the land. When the land starts to cools in the fall the
432 MSE maximum at first gradually shifts southwards, until the strong winds reappear and the max-
433 imum MSE jumps southwards. The jumps are clearer in the simulations without the interactive
434 OHT because removing the link between OHT and the surface winds reduces the variability of the
435 precipitation and also makes the model less likely to have a double-ITCZ.

436 These results have been obtained with an idealized model, but demonstrate the substantial impact
437 OHT can have on the monsoonal circulation, both through the zonal-mean effect of the atmosphere
438 needing to transport less heat across the equator and through the local effect of creating a stronger
439 meridional MSE gradient. Work with more realistic models, which include realistic topography, is
440 required to fully quantify the impact these effects have on the South Asian Monsoon. Furthermore,
441 as has been noted in several previous studies, a theory for the compensation between the ocean
442 and the atmosphere is required in order to quantitatively predict how the overturning circulation
443 is affected by the increased OHT, particularly a theory for how the gross moist stability of the
444 tropical atmosphere is affected.

445 The Indian subcontinent seems to be ideally situated to develop a strong monsoon, being insu-
446 lated from cold winds blowing down from Eurasia by the Himalayas to the north, while to the
447 south the northern Indian Ocean transports heat southwards, cooling the SSTs off the coast of In-
448 dia and further enhancing the meridional MSE gradient. A better understanding of the roles each
449 of these features play in setting up the monsoon, and of how they interact with each other, will be
450 required for a complete picture of the South Asian Monsoon.

451 *Acknowledgment.* We thank Peter Webster and Tim Cronin for helpful discussions. Nicholas
452 Lutsko was partly supported by NSF grant AGS-1623218, “Collaborative Research: Using a Hi-
453 erarchy of Models to Constrain the Temperature Dependence of Climate Sensitivity”.

454 References

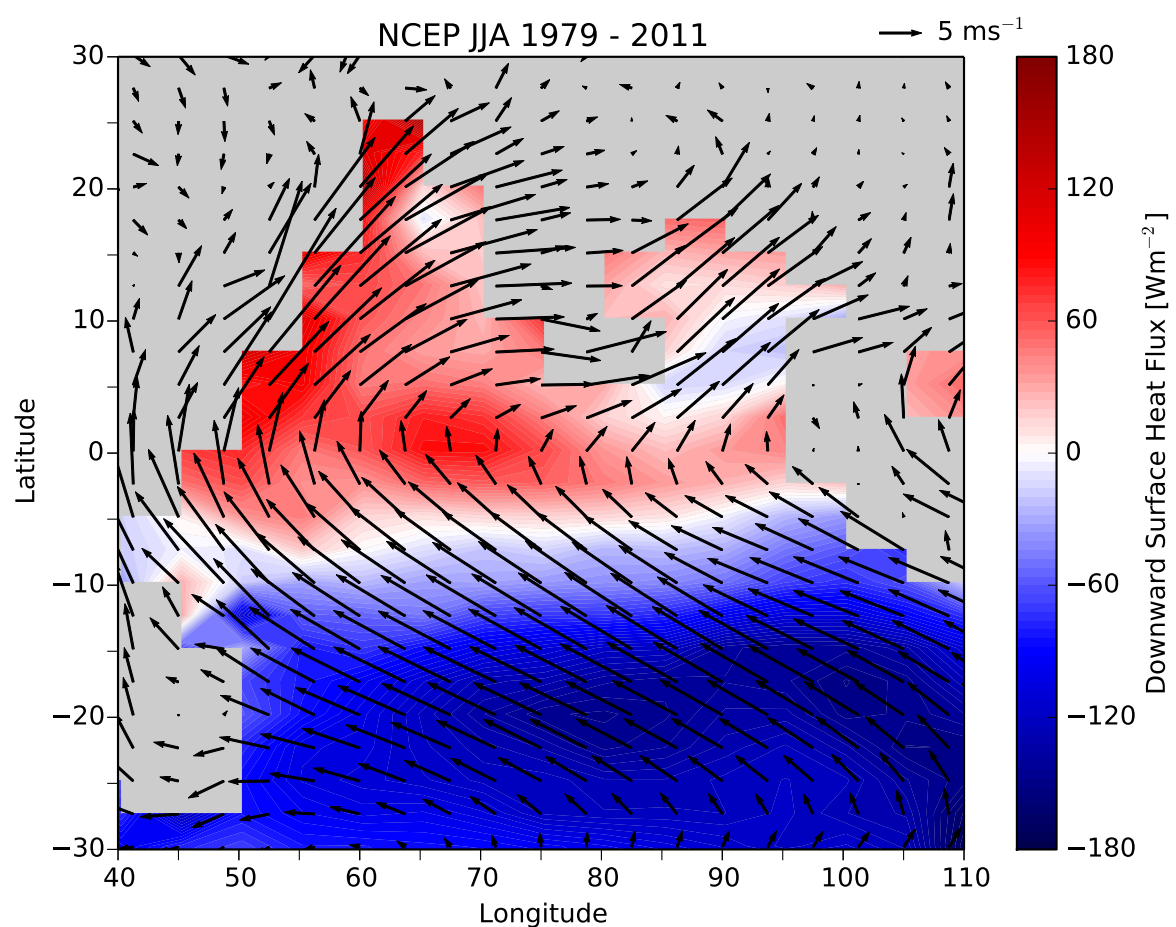
455 Babu, K. N., R. Sharma, N. Agarwal, A. V. K., and W. R. A., 2004: Study of the mixed layer depth
456 variations within the north indian ocean using a 1d model. *Journal of Geophysical Research:*
457 *Oceans*, **109 (C8)**.

- 458 Bischoff, T., and T. Schneider, 2016: The equatorial energy balance, itcz position, and double itcz
459 bifurcations. *Journal of Climate*, **29** (15), 2997–3013.
- 460 Boos, W. R., and Z. Kuang, 2010: Dominant control of the south asian monsoon by orographic
461 insulation versus plateau heating. *Nature*, **463** (23), 218–222.
- 462 Bordoni, S., and T. Schneider, 2008: Monsoons as eddy-mediated regime transitions of the tropical
463 overturning circulation. *Nature Geoscience*, **1** (23), 515–519.
- 464 Chirokova, G., and P. J. Webster, 2006: Interannual variability of indian ocean heat transport.
465 *Journal of Climate*, **19** (6), 1013–1031.
- 466 Chou, C., J. D. Neelin, and H. Su, 2001: Ocean-atmosphere-land feedbacks in an idealized mon-
467 soon. *Quarterly Journal of the Royal Meteorological Society*, **127** (15), 1869–1891.
- 468 Codron, F., 2012: Ekman heat transport for slab oceans. *Climate Dynamics*, **38** (1), 379–389.
- 469 Czaja, A., and J. Marshall, 2005: The partitioning of poleward heat transport between the atmo-
470 sphere and ocean. *Journal of the Atmospheric Sciences*, **63**, 1498–1511.
- 471 Donohoe, A., D. M. W. Frierson, and D. S. Battisti, 2014: The effect of ocean mixed layer depth
472 on climate in slab ocean aquaplanet experiments. *Climate Dynamics*, **43** (3), 1041–1055.
- 473 Emanuel, K. A., 1995: On thermally direct circulations in moist atmospheres. *Journal of the*
474 *Atmospheric Sciences*, **52** (15), 1529–1534.
- 475 Frierson, D. M. W., 2007: The dynamics of idealized convection schemes and their effect on the
476 zonally averaged tropical circulation. *Journal of the Atmospheric Sciences*, **64** (23), 1959–1976.
- 477 Frierson, D. M. W., I. M. Held, and P. Zurita-Gotor, 2006: A gray-radiation aquaplanet moist gcm.
478 part i: Static stability and eddy scales. *Journal of the Atmospheric Sciences*, **63** (23), 2548–2566.

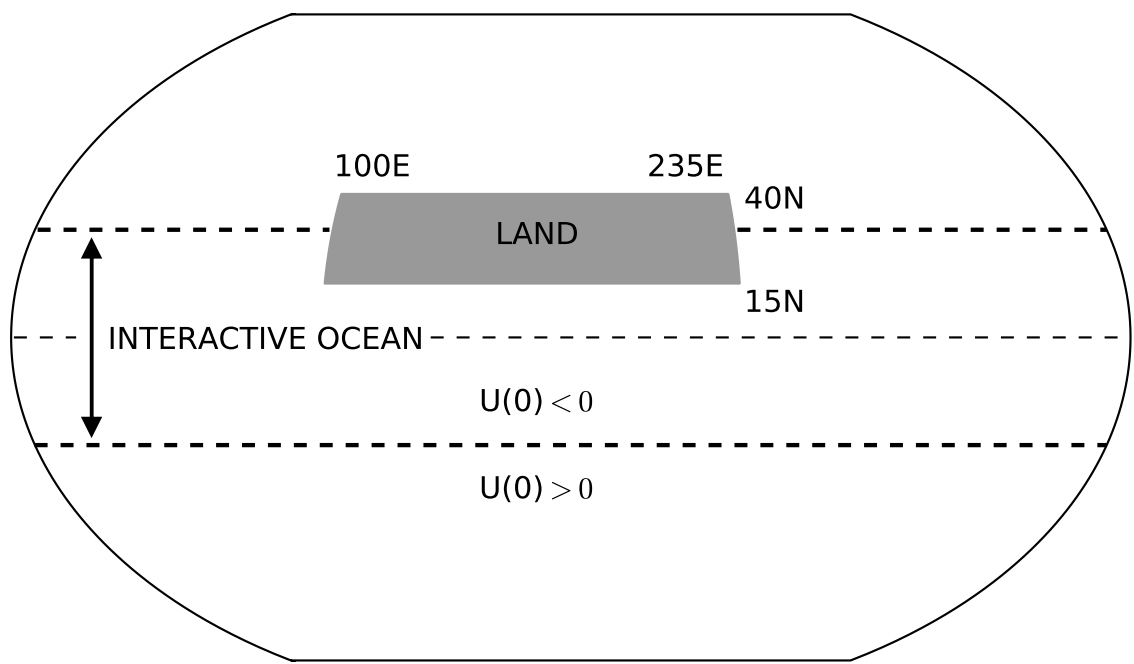
- 479 Geen, F., F. H. Lambert, and G. K. Vallis, 2018: Regime change behavior during asian monsoon
onset. *Journal of Climate*, **31** (9), 3327–3348.
- 481 Green, B., and J. Marshall, 2017: Coupling of trade winds with ocean circulation damps itcz shift.
482 *Journal of Climate*, **30** (12), 4395–4411.
- 483 Hartmann, D. L., 2016: *Global Physical Climatology*. 2nd ed., Elsevier.
- 484 Held, I. M., 2001: The partitioning of the poleward energy transport between the tropical ocean
485 and atmosphere. *Journal of the Atmospheric Sciences*, **58**, 943–948.
- 486 Klinger, B. A., and J. Marotzke, 2000: Meridional heat transport by the subtropical cell. *Journal*
487 *of Physical Oceanography*, **30** (23), 696–705.
- 488 Levine, X. J., and T. Schneider, 2011: Response of the hadley circulation to climate change in
489 an aquaplanet gcm coupled to a simple representation of ocean heat transport. *Journal of the*
490 *Atmospheric Sciences*, **68** (8), 769–783.
- 491 Levitus, S., 1987: Meridional ekman heat fluxes for the world ocean and individual ocean basins.
492 *Journal of Physical Oceanography*, **17** (23), 1484–1492.
- 493 Loschnigg, J., and P. J. Webster, 2000: A coupled oceanatmosphere system of sst modulation for
494 the indian ocean. *Journal of Climate*, **13** (104), 3342–3360.
- 495 Ma, D., W. R. Boos, and Z. Kuang, 2014: Effects of orography and surface heat fluxes on the
496 south asian summer monsoon. *Journal of Climate*, **27** (9), 6647–6659.
- 497 McCreary, J. P., P. K. Kundu, and R. L. Molinari, 1993: A numerical investigation of the dynamics,
498 thermodynamics and mixed layer processes in the indian ocean. *Progress in Oceanography*,
499 **31** (23), 181–244.

- 500 O’Gorman, P. A., and T. Schneider, 2008: The hydrological cycle over a wide range of climates
501 simulated with an idealized gcm. *Journal of Climate*, **21** (15), 3815–3832.
- 502 Pauluis, O., 2004: Boundary layer dynamics and cross-equatorial hadley circulation. *Journal of*
503 *the Atmospheric Sciences*, **61** (23), 1161–1173.
- 504 Plumb, R. A., and A. Y. Hou, 1992: The response of a zonally symmetric atmosphere to sub-
505 tropical thermal forcing: Threshold behavior. *Journal of the Atmospheric Sciences*, **49** (23),
506 1790–1799.
- 507 Privé, N. C., and R. A. Plumb, 2007a: Monsoon dynamics with interactive forcing. part i: Ax-
508 isymmetric studies. *Journal of the Atmospheric Sciences*, **64** (23), 1417–1430.
- 509 Privé, N. C., and R. A. Plumb, 2007b: Monsoon dynamics with interactive forcing. part ii: Impact
510 of eddies and asymmetric geometries. *Journal of the Atmospheric Sciences*, **64** (23), 1431–1442.
- 511 Schneider, T., 2017: Feedback of atmosphere-ocean coupling on shifts of the intertropical conver-
512 gence zone. *Geophysical Research Letters*, **44** (12), 11 644–11 653.
- 513 Schott, F. A., S.-P. Xie, and J. P. McCreary, 2009: Indian ocean circulation and climate variability.
514 *Reviews of Geophysics*, **47** (1).
- 515 Singh, M. S., Z. Kuang, and Y. Tian, 2017: Eddy influences on the strength of the hadley circula-
516 tion: Dynamic and thermodynamic perspectives. *Journal of the Atmospheric Sciences*, **74** (15),
517 467–486.
- 518 Sobel, A., J. Nilsson, and L. M. Polvani, 2001: The weak temperature gradient approximation and
519 balanced tropical moisture waves. *Journal of the Atmospheric Sciences*, **58**, 3650–3665.
- 520 Vecchi, G. A., and D. E. Harrison, 2002: Monsoon breaks and subseasonal sea surface temperature
521 variability in the bay of bengal. *Journal of Climate*, **15** (1), 1485–1493.

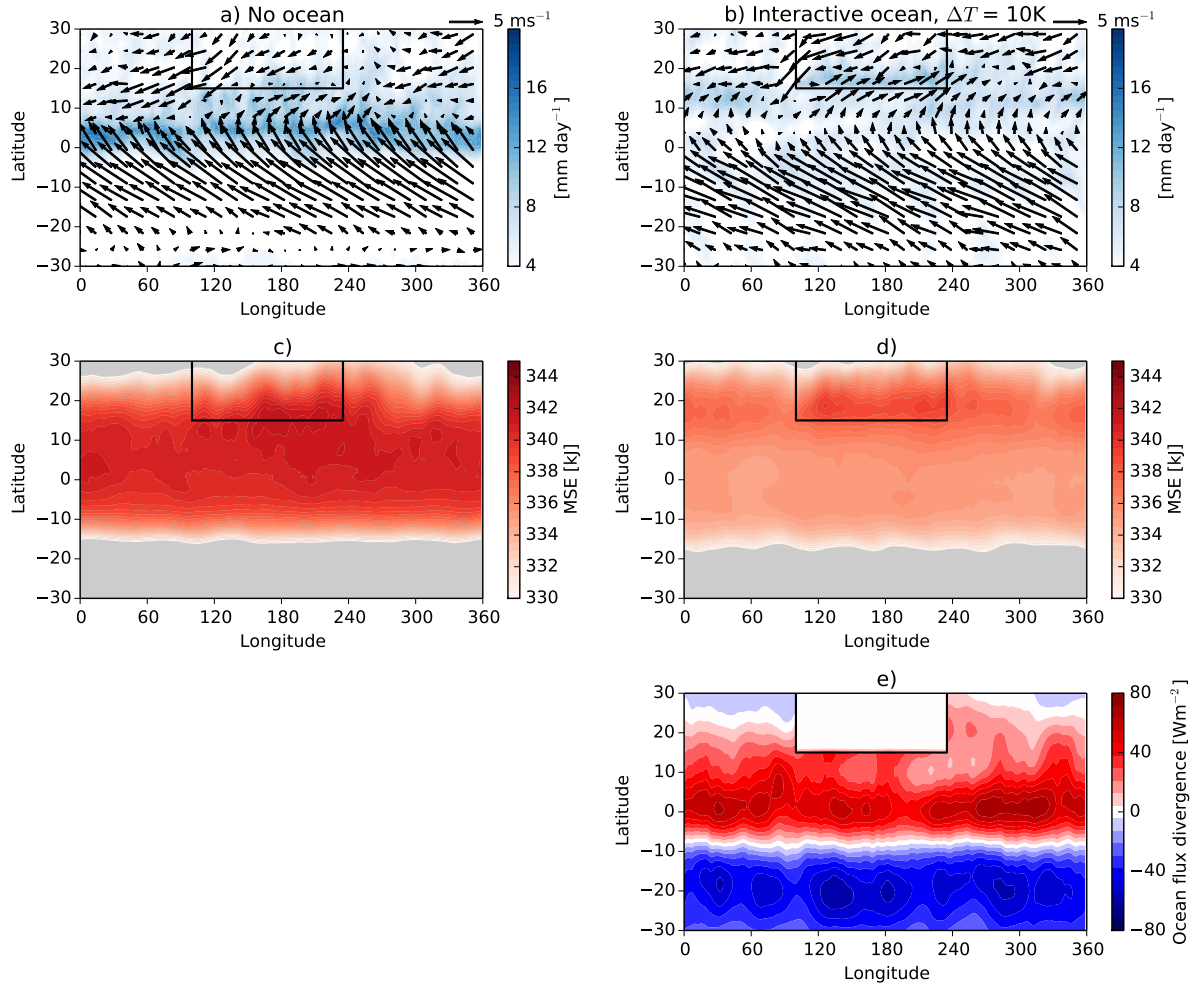
- 522 Walker, C. C., and T. Schneider, 2006: Eddy influences on hadley circulations: Simulations with
523 an idealized gcm. *Journal of the Atmospheric Sciences*, **63** (15), 3333–3350.
- 524 Webster, P. J., C. Clark, G. Cherikova, J. Fasulla, W. Han, J. Loschnigg, and K. Sahami, 2002:
525 The monsoon as a self-regulating coupled oceanatmosphere system. *International Geophysics*,
526 **83** (2), 198–219.
- 527 Webster, P. J., and S. Yang, 1992: Monsoon and enso: Selectively interactive systems. *Quarterly
528 Journal of the Royal Meteorological Society*, **118** (23), 877–926.
- 529 Zhai, J., and W. Boos, 2015: Regime transitions of cross-equatorial hadley circulations with zon-
530 ally asymmetric thermal forcings. *Journal of the Atmospheric Sciences*, **64** (23), 3800–3818.



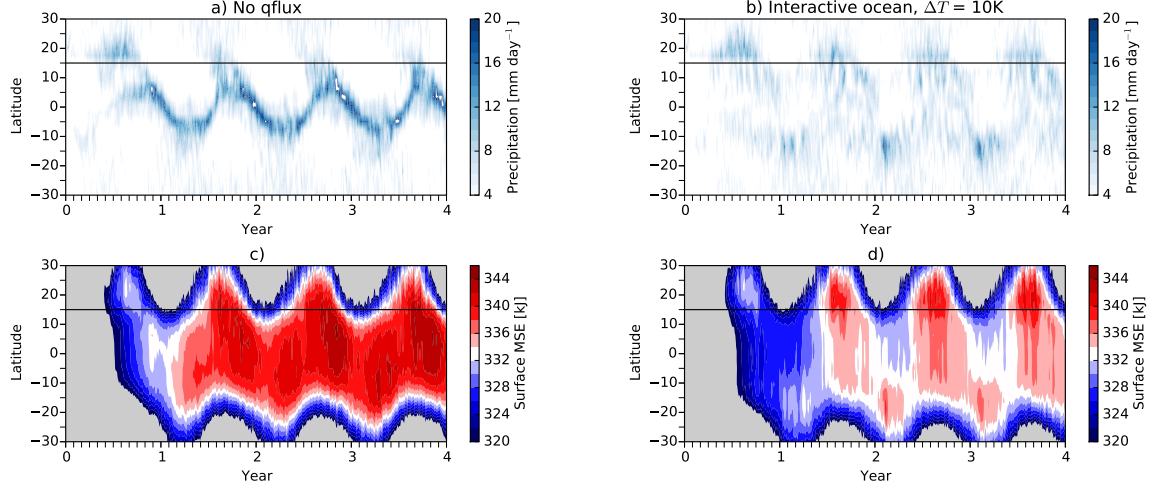
531 FIG. 1. Climatological June-July-August (JJA) downward energy flux at the ocean surface (contours) and
 532 surface winds (arrows) from the NCEP reanalysis for the period 1979 to 2011.



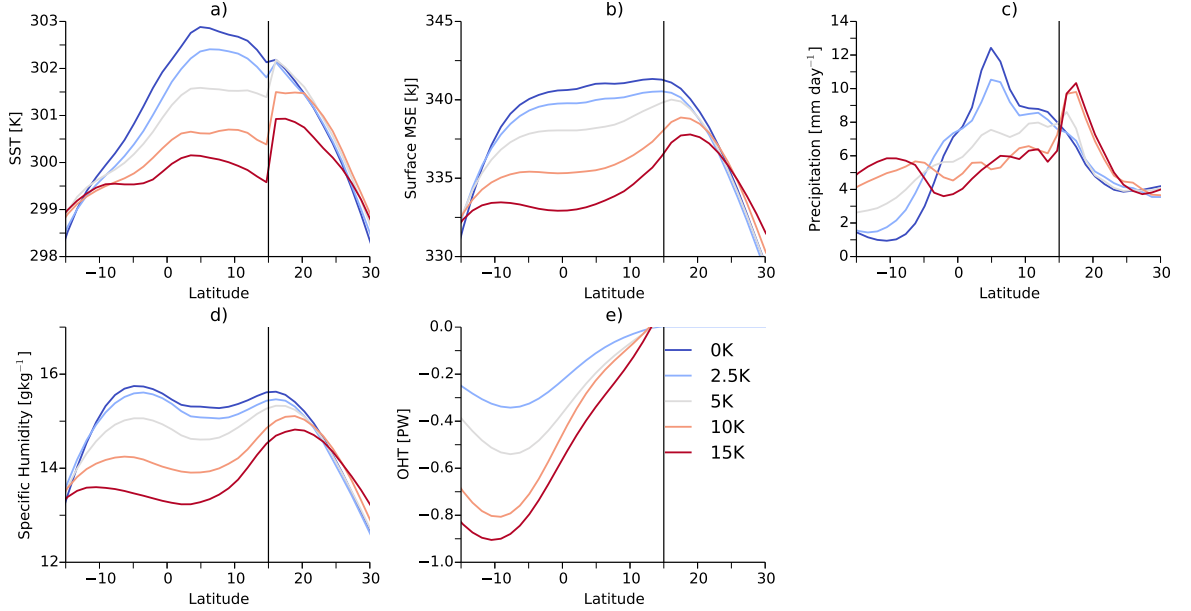
533 FIG. 2. Schematic of the model configuration used in the experiments. Note that the boundaries of the
534 interactive ocean move seasonally.



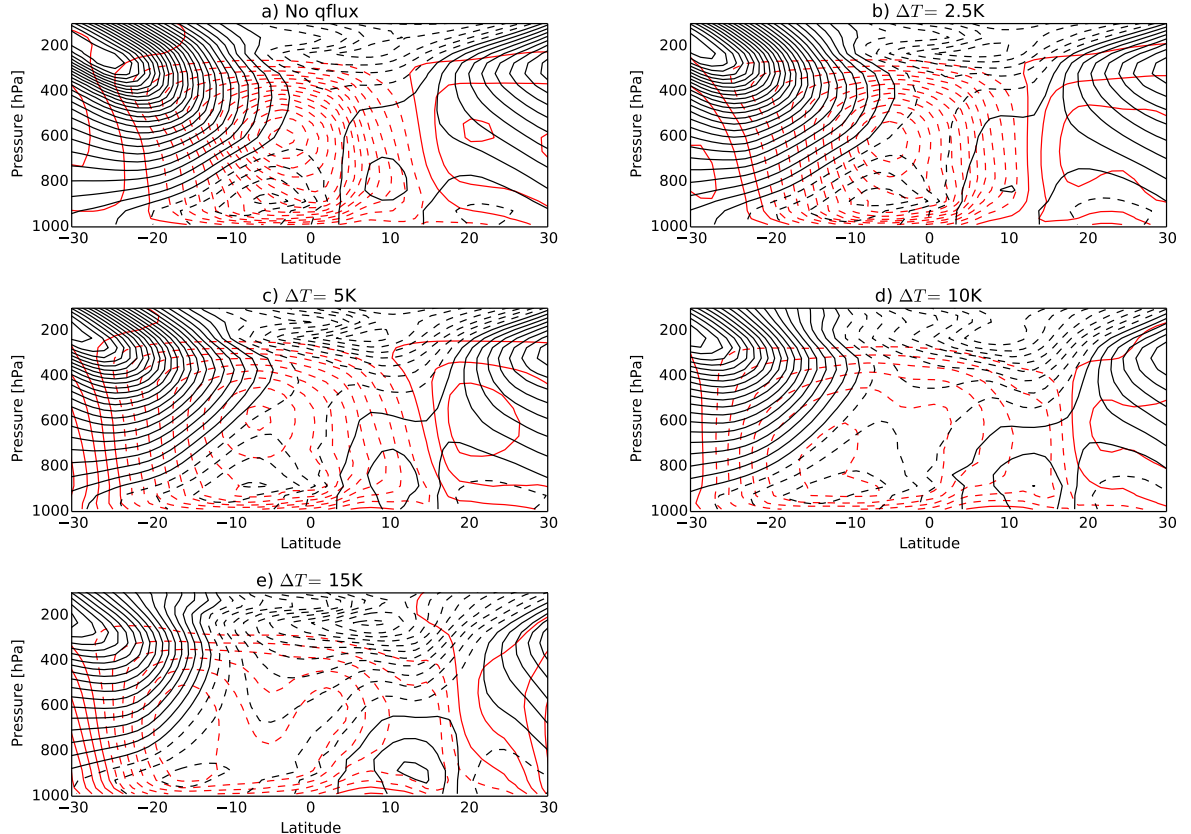
535 FIG. 3. a), b) Summer-time precipitation (blue contours) and winds at the lowest model level (arrows) for the
 536 experiment with no OHT (a) and the experiment with interactive OHT and $\Delta T = 10K$ (b). c), d) Moist static
 537 energy (MSE) at the lowest model level from the same experiments. Gray regions have MSE values outside the
 538 colorbar scale. e) OHT divergence from the experiment with interactive OHT.



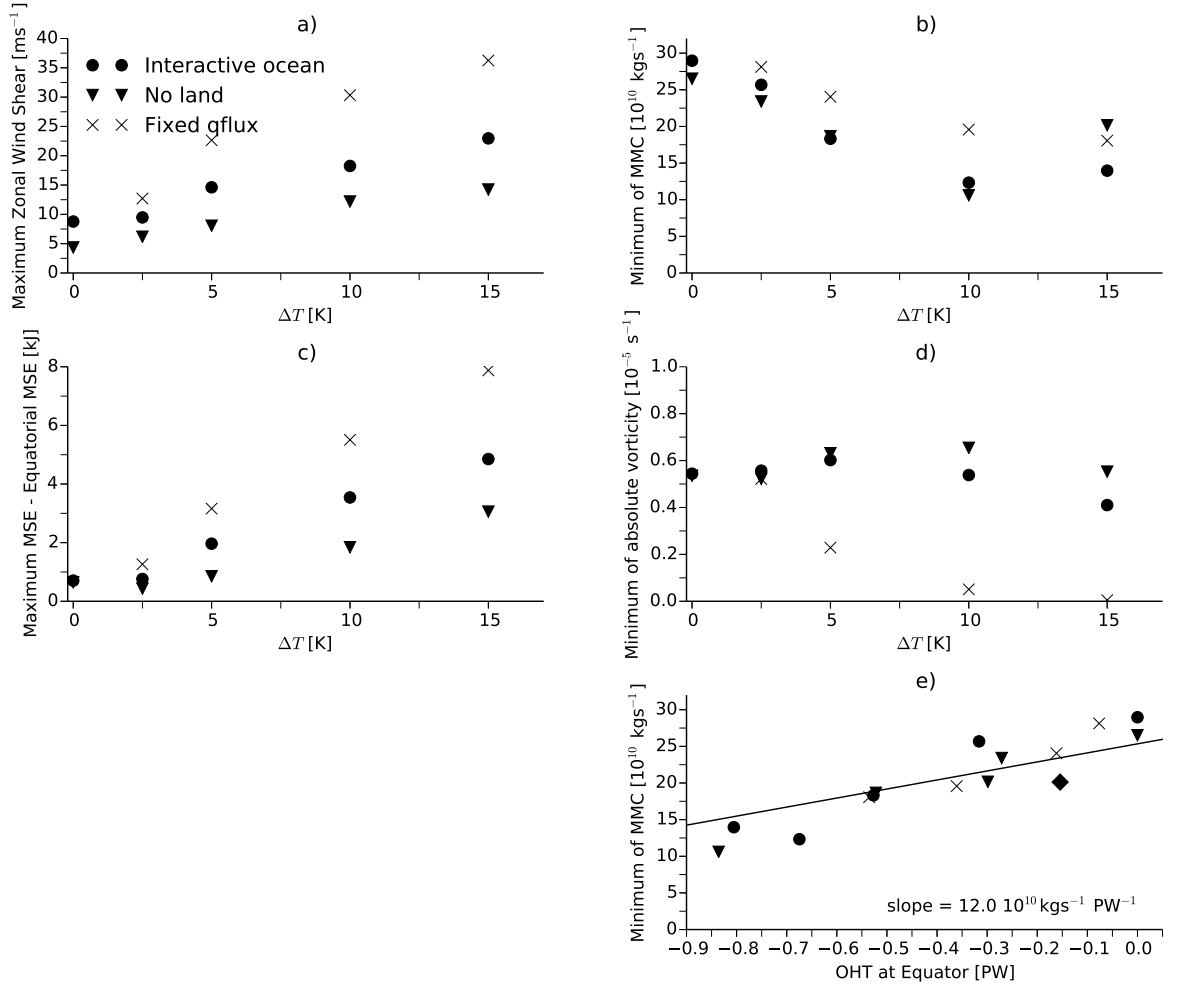
539 FIG. 4. a), c) Hovmuller diagrams of the precipitation (a) and surface MSE (c), averaged over 100° to 235° E,
 540 for the land simulation with no OHT. b), d) Same for the land simulation with interactive OHT and $\Delta T = 10K$.
 541 The horizontal black lines mark the southern edge of the continent. Note that the model is initialized at year 0.



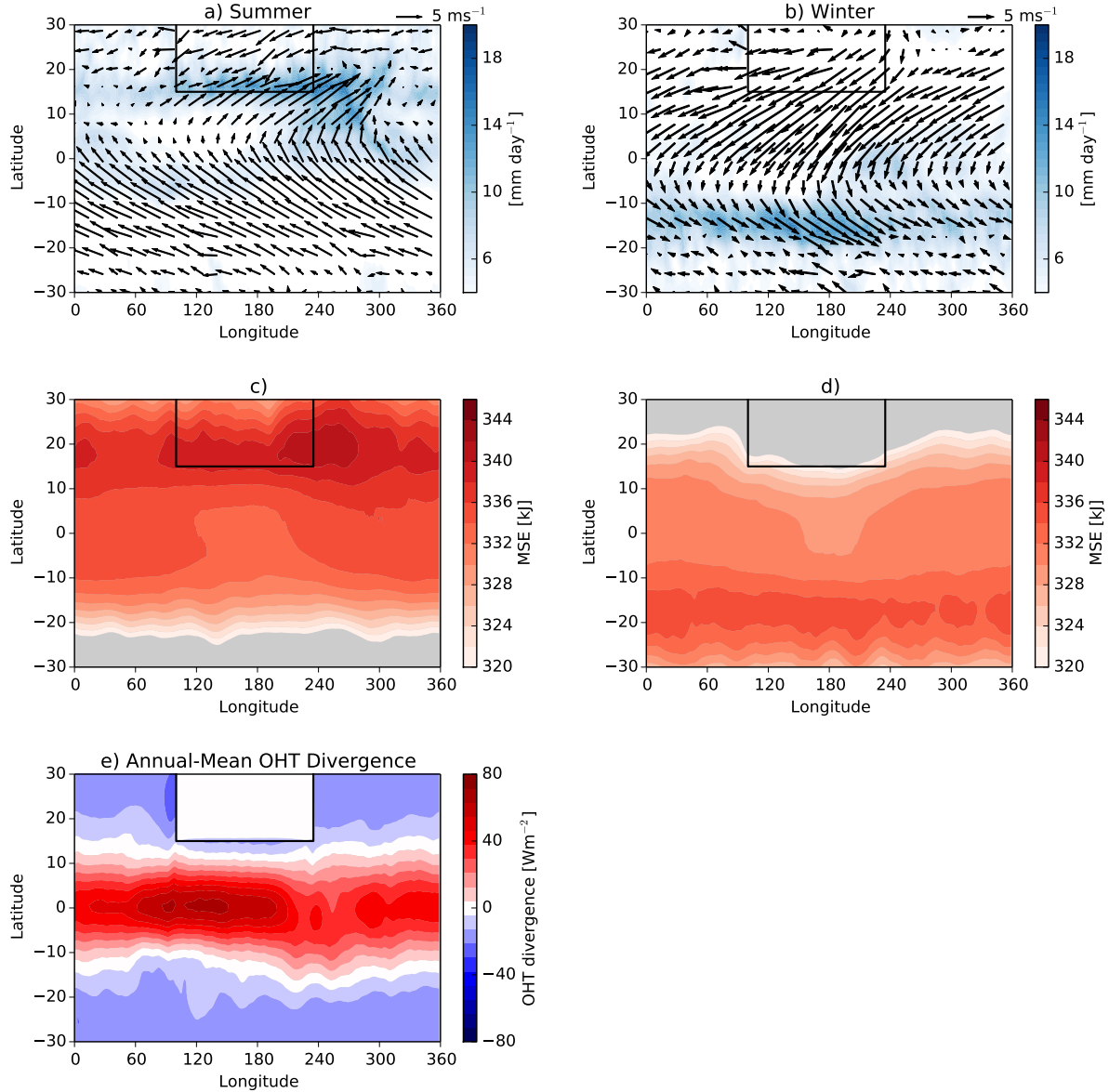
542 FIG. 5. a) Summer SSTs, averaged from 100° to 235° E, in the simulations with land and with ΔT varied
 543 from 0K to 15K. The vertical line marks the southern boundary of the continent. b) Averaged summer surface
 544 MSE in these simulations. c) Averaged summer precipitation in these simulations. d) Averaged summer specific
 545 humidity in these simulations. e) Averaged summer OHT in these simulations.



546 FIG. 6. a) Summertime mean meridional circulation (MMC, red contours) and zonal winds (black contours)
 547 averaged over the land sector (100° to 235°E) in the land simulation with $\Delta T = 0\text{K}$. The contour intervals are 2
 548 $\times 10^9 \text{kg s}^{-1}$ for the MMC and 2ms^{-1} for the zonal wind. Dashed red contours denote counterclockwise circula-
 549 tion and dashed black contours denote negative zonal wind speeds. b) Same for the simulation with $\Delta T = 2.5\text{K}$.
 550 c) Same for the simulation with $\Delta T = 5\text{K}$. d) Same for the simulation with $\Delta T = 10\text{K}$. e) Same for the simulation
 551 with $\Delta T = 15\text{K}$.



552 FIG. 7. a) Maximum of $(u(850\text{hPa}) - u(250\text{hPa}))$, averaged over the land sector (100° to 235°E), between
 553 the equator and 20°N during the summer months for the simulations with land and interactive OHT (circles),
 554 the simulations with interactive OHT and no land (triangles) and with land and OHT fixed at its annual-mean
 555 values (crosses). b) Minimum of the summertime mean meridional circulation (MMC) for the same simulations.
 556 c) Difference between maximum summer MSE and equatorial MSE at the equator for the same simulations. d) Minimum absolute vorticity polewards of 7°N during the summer of the same simulations. e) Minimum of the
 557 summertime MMC for the same simulations as a function of the equatorial OHT in the land sector. The line
 558 shows a linear least-squares fit.



560 FIG. 8. a) Summer precipitation (contours) and near-surface winds (arrows) in the simulation with land and
 561 OHT fixed at its annual-mean value from the ΔT simulation with land. c) Summer near-surface MSE from the
 562 same simulation. b), d) Winter precipitation and near-surface MSE from the same simulation. e) Annual-mean
 563 OHT divergence in the $\Delta T = 10\text{K}$ simulation with land.

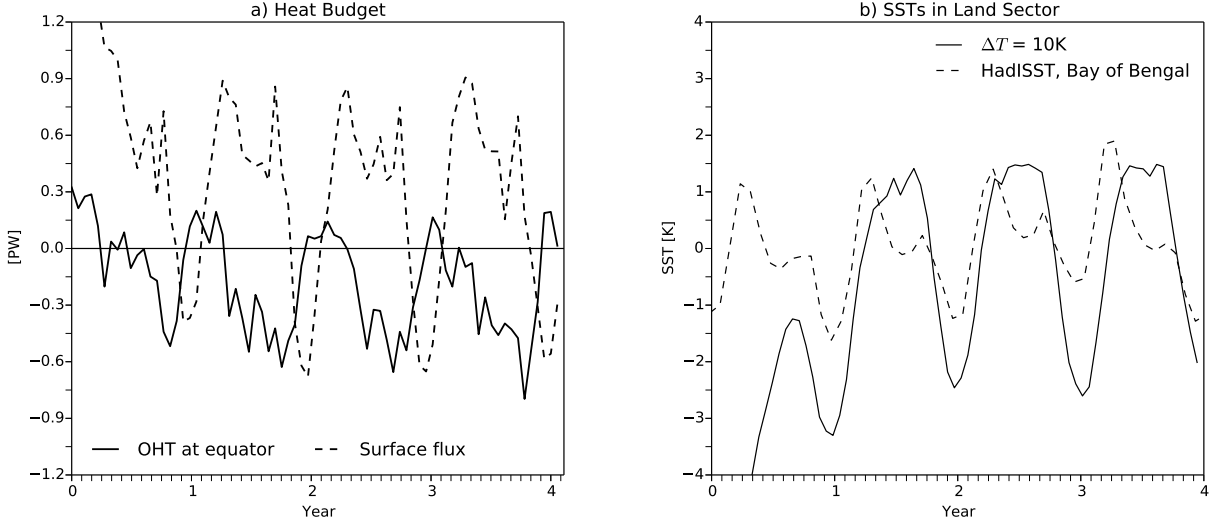


FIG. 9. a) Ocean heat transport across the equator, integrated from 100° to 235° E (solid line) and net surface flux integrated over the region 100° to 235° E and 0 to 15° N, from the land simulation with $\Delta T = 10K$ (dashed line). The heat transport is positive when it is northward. b) SSTs averaged over the region (100° to 235° E and 0° to 15° N) from the simulation with $\Delta T = 10K$ (solid line) and SSTs averaged over the Bay of Bengal (80° to 95° E and 0° to 15° N) for the period 2012 to 2016, taken from the HadISST dataset.

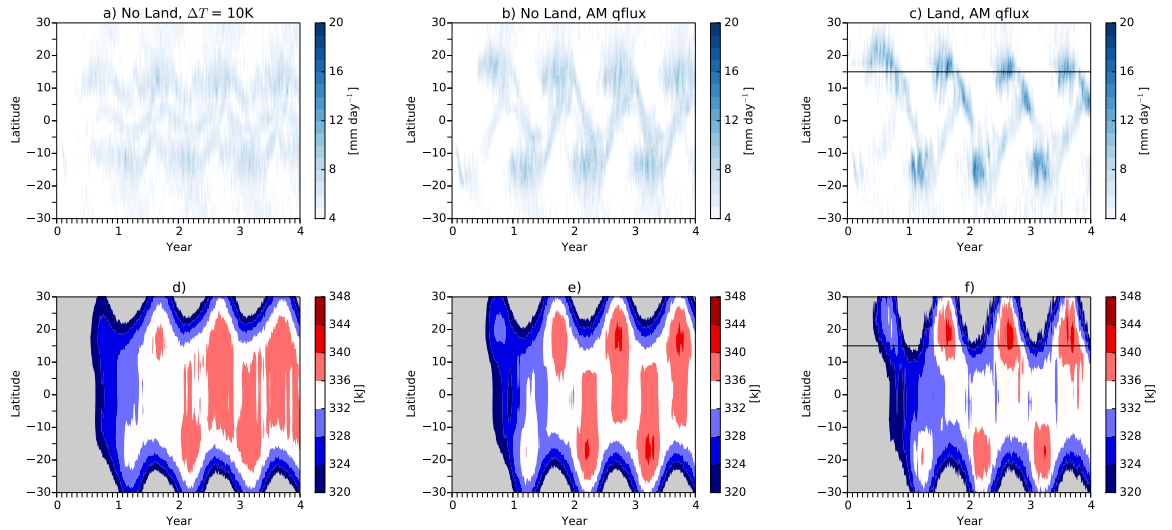


FIG. 10. a), d) Hovmuller diagrams of zonal-mean precipitation (a) and meridional gradient of surface MSE (d) for the simulation with no land and $\Delta T = 10K$. b), e) Same for the simulation without land and with OHT fixed at its annual-mean value from the $\Delta T = 10K$ simulation. c), f) Same for the simulation with land and with OHT fixed at its annual-mean value from the $\Delta T = 10K$ simulation.